Spatially dispersive circular photogalvanic effect in a Weyl semimetal

Zhurun Ji^{1,5}, Gerui Liu^{1,5}, Zachariah Addison², Wenjing Liu¹, Peng Yu³, Heng Gao¹, Zheng Liu³, Andrew M. Rappe⁴, Charles L. Kane², Eugene J. Mele² and Ritesh Agarwal¹

Weyl semimetals (WSMs) are gapless topological states of matter with broken inversion and/or time reversal symmetry. WSMs can support a circulating photocurrent when illuminated by circularly polarized light at normal incidence. Here, we report a spatially dispersive circular photogalvanic effect (s-CPGE) in a WSM that occurs with a spatially varying beam profile. Our analysis shows that the s-CPGE is controlled by a symmetry selection rule combined with asymmetric carrier excitation and relaxation dynamics. By evaluating the s-CPGE for a minimal model of a WSM, a frequency-dependent scaling behaviour of the photocurrent is obtained. Wavelength-dependent measurements from the visible to mid-infrared range show evidence of Berry curvature singularities and band inversion in the s-CPGE response. We present the s-CPGE as a promising spectroscopic probe for topological band properties, with the potential for controlling photoresponse by patterning optical fields on topological materials to store, manipulate and transmit information.

SMs are a family of gapless topological materials with Weyl nodes, that is, momentum-space monopole and antimonopole singularities of the Berry curvature of the bulk Bloch band. Due to their unique band structures, there has been interest in understanding their electronic and transport properties¹⁻¹². Recently, these studies have been extended to explore their optical properties, especially through the measurement of nonlinear responses. Most experiments have focused on type-I WSMs such as tantalum arsenide, where a zero-bias photocurrent under chiral optical excitation at mid-infrared frequencies13 has been attributed to the distinct chirality of each tilted Weyl cone, and exceedingly large values of the second-order nonlinear optical susceptibility at visible frequencies have been observed14. Some progress has also been made to theoretically understand the nature of injection photocurrents in WSMs15-19 by using two-band models to capture the essential physics in the vicinity of Weyl nodes.

WSMs are representatives of a wide class of materials that combine inversion or time reversal symmetry breaking along with spin-orbit coupling. In these materials, optical excitation can lead to asymmetric carrier excitation and relaxation pathways and generate new photocurrent responses. However, these properties have not been experimentally investigated due to the lack of probes that are particularly sensitive to such asymmetries. Here, we observe a circulating photocurrent driven by a spatially inhomogeneous optical field in type-II inversion-symmetrybroken WSMs, molybdenum tungsten ditelluride (Mo_xW_{1-x}Te₂) when x=0.3 and 0.9, and MoTe₂, where we find that the photocurrent is controlled both by the spatial profile and polarization of the exciting field. By deriving the response functions that govern the frequency-dependent s-CPGE and performing experiments over a large spectral range (visible to mid-infrared excitation), we demonstrate the capabilities of the s-CPGE for studying topological band properties and asymmetric carrier relaxation in topological materials.

Following the discovery of MoTe₂ as an inversion-symmetry-broken type-II WSM below 250 K (refs. 20,21), tungsten-doped ternary alloys, Mo_xW_{1-x}Te₂ when x>0.07 have also been demonstrated as room-temperature type-II WSMs^{22,23}. Bulk MoTe₂ has three different crystal phases: hexagonal 2H, monoclinic 1T' (*P*2₁/*m* space group, Fig. 1a) and orthorhombic T_d (*Pmn*2₁, Fig. 1b). Studies have shown that it has a phase transition at ~250 K from a high-temperature trivial centrosymmetric semimetal 1T' phase to a low-temperature inversion-symmetry-broken WSM T_d phase²⁴. These two structures have different atomic stacking along the *c* axis, but share the same in-plane symmetry. Likewise, Mo_{0.3}W_{0.7}Te₂ and Mo_{0.9}W_{0.1}Te₂ are room-temperature inversion-broken WSMs with the same crystal structure as T_d-phase MoTe₂.

Bulk crystals of MoTe₂ and Mo_xW_{1-x}Te₂ (x=0.3 and 0.9) were grown via a chemical vapour transport technique (see Methods and Supplementary Fig. 1), and have been shown to be inversion-broken WSMs^{25,26}. Photocurrent measurements were performed by varying the spot size, location and polarization of a Gaussian profile laser beam, with wavelengths ranging from 750 nm to 6.2 μ m, propagating along the crystal growth direction (c axis), which we assign as the \hat{z} axis in the laboratory frame. Polarization- and position-dependent photocurrent measurements were performed using a homebuilt optical microscopy cryostat set-up (Fig. 1c) (see Methods)²⁷ at zero bias under low optical powers (<12 mW) to ensure that the photocurrent scaled linearly with power (Supplementary Fig. 2).

To isolate the special properties of the photogalvanic effect (PGE) hosted in the inversion-broken low-temperature phase of MoTe₂, photocurrent measurements were compared at both 300 K (that is, in the 1T' phase with inversion symmetry) and 77 K (T_d phase with broken inversion symmetry) on exfoliated flakes with microfabricated electrodes (see Methods), with a 750 nm laser. Photocurrents were measured at two different spots (for example, locations a and b in Fig. 1c) along the bisector of the electrodes as a function of the rotation angle of the fast axis of the quarter-wave plate, φ , with respect to

¹Department of Materials Science and Engineering, University of Pennsylvania, Philadelphia, PA, USA. ²Department of Physics and Astronomy, University of Pennsylvania, Philadelphia, PA, USA. ³Centre for Programmable Materials, School of Materials Science and Engineering, Nanyang Technological University, Singapore, Singapore. ⁴Department of Chemistry, University of Pennsylvania, Philadelphia, PA, USA. ⁵These authors contributed equally: Zhurun Ji, Gerui Liu. *e-mail: riteshag@seas.upenn.edu

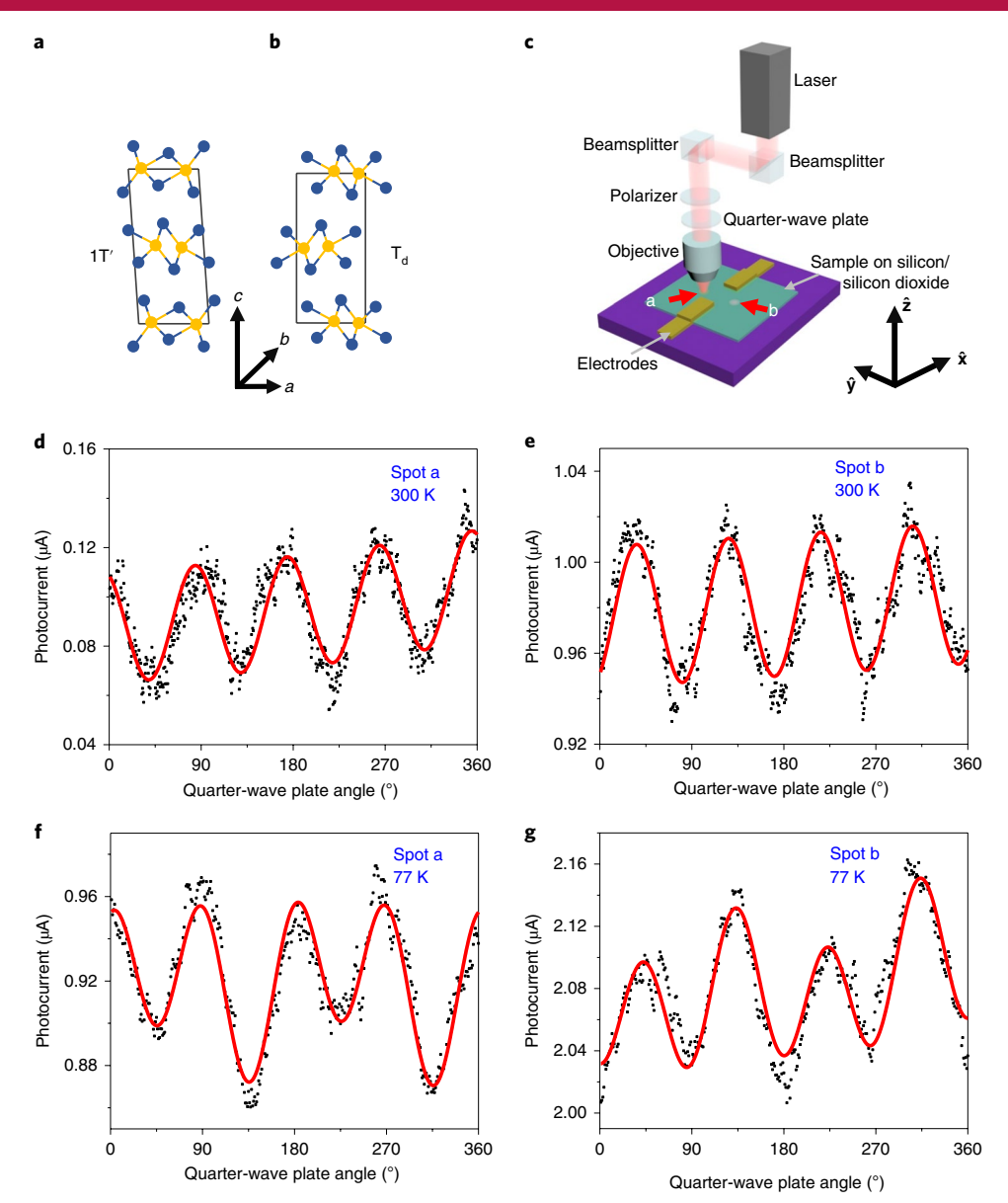


Fig. 1 | **Polarization-dependent photocurrent measurements on 1T'** and T_d (**Weyl) phases of MoTe₂. a,b**, Crystal structures of the 1T' (**a**) and T_d phase of MoTe₂ (**b**). Yellow (blue) spheres represent Mo (Te) atoms, and a, b and c are the crystallographic axes. **c**, Schematic of the polarization-dependent photocurrent measurement set-up. In all our experiments, a Gaussian laser beam propagating along the $\hat{\mathbf{z}}$ axis was focused by a microscope objective incident normally onto the sample ($\hat{\mathbf{x}} - \hat{\mathbf{y}}$ plane), with the $\hat{\mathbf{z}}$ axis parallel to the crystallographic c axis of MoTe₂. \mathbf{d} - \mathbf{g} , Photocurrent plotted as a function of φ at two spatial locations and temperatures: spot a at 300 K (\mathbf{d}); spot b at 300 K (\mathbf{e}); spot a at 77 K (\mathbf{f}); spot b at 77 K (\mathbf{g}). Black dots are the experimental data, and red lines are the fits to equation (1).

the linear polarization of the incident laser. The photocurrent measured from MoTe₂ at spot a and at 300 K shows some linear polarization dependence (Fig. 1d), but it has nearly the same magnitude at $\varphi=45^\circ$ (left circular polarization) and 135° (right circular polarization), implying that light with opposite helicities produce similar photocurrents and hence no CPGE. However, at 77 K (Fig. 1f), the photocurrent magnitude in the Weyl phase of MoTe₂ at $\varphi=45^\circ$ is much larger than for $\varphi=135^\circ$, showing a strong dependence on the light helicity. Curiously, the circular polarization-dependent part of the photocurrent at spot b (Fig. 1e,g) has an opposite polarity compared with spot a, indicating also a position-dependent response.

The differences between the PGE from MoTe₂ in its two phases and its unusual spatial dependence are quantified using a phenomenological expression for the photocurrents. First, the observed photocurrents from the sample were fitted to the equation

Table 1 | Fitting parameters for polarization-dependent photocurrent data measured on MoTe₂ at two spatial locations (a and b) at two temperatures

MoTe ₂	Spot a		Spot b	
	J _L (nA)	J _c (nA)	J_{L} (nA)	J _c (nA)
300 K (1T′)	23	~0	-30	~0
77 K (T _d)	34	14	-40	-21
The data are shown in Fig. 1d-g and are fitted using equation (1).				

$$J = J_{\rm C} \sin(2\varphi) + J_{\rm L} \sin(4\varphi + \varphi_0) + J_0 \tag{1}$$

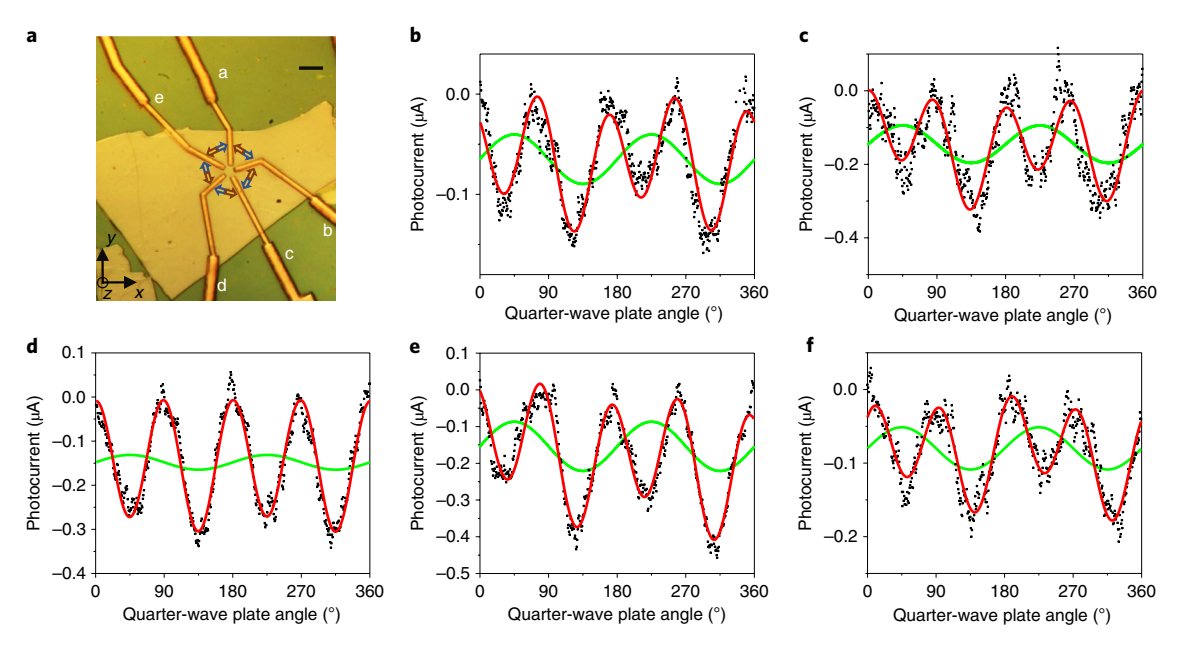


Fig. 2 | Measurement of circulating current in the \mathbf{T}_d (Weyl) phase of $\mathbf{Mo}_{0.9}\mathbf{W}_{0.1}\mathbf{Te}_2$ at room temperature under circularly polarized optical excitation. **a**, Optical image of the multi-electrode $\mathbf{Mo}_{0.9}\mathbf{W}_{0.1}\mathbf{Te}_2$ device ($\hat{\mathbf{x}}-\hat{\mathbf{y}}$ plane). The five electrodes are labelled a-e, and red and blue arrows indicate the circulating direction of the CPGE current under LCP and RCP light illumination (spot size $\approx 2 \, \mu \text{m}$), respectively. Scale bar: 5 μm. **b-f**, Photocurrents are measured between each of the nearest electrode pairs and plotted as functions of φ . Plots correspond to measurements performed between electrodes $\mathbf{a} \rightarrow \mathbf{b}$ (\mathbf{b}), $\mathbf{b} \rightarrow \mathbf{c}$ (\mathbf{c}), $\mathbf{c} \rightarrow \mathbf{d}$ (\mathbf{d}), $\mathbf{d} \rightarrow \mathbf{e}$ (\mathbf{e}) and $\mathbf{e} \rightarrow \mathbf{a}$ (\mathbf{f}). Black dots are the experimental data, red lines are the fitted curves for total photocurrent (equation (1)) and the green lines represent the fitted CPGE currents.

where I_C is the magnitude of the CPGE current, I_L is the magnitude of the linear photogalvanic effect (LPGE) current with phase shift φ_0 and J_0 is the polarization-independent background current. In the experiments, I_0 achieves its extrema at the ends of the electrodes and always vanishes near the midpoint (Supplementary Fig. 3), which implies that it is mostly a result of the Dember effect due to the heat gradients induced by asymmetric illumination on the electrodes/ sample²⁸. Fitting the total photocurrent *J* to our experimental results (Table 1) shows that J_1 exists at both temperatures with similar magnitudes. However, J_C is approximately zero at 300 K, but is easily observed at 77 K, and is reversible with temperature. Meanwhile, both J_C and J_L have opposite polarities at spots a and b, which is strikingly different from a conventional PGE. Furthermore, from symmetry considerations, in both the T_d -phase ($C_{2\nu}$ symmetry) and 1T'-phase (C_{2h}) MoTe₂, under normally incident light on the $\hat{\mathbf{x}} - \hat{\mathbf{y}}$ plane (propagation direction, $\hat{\mathbf{z}}$), any in-plane second-order optical response such as a PGE^{29,30} or photon drag effect³¹ is forbidden by the two-fold rotation symmetry. Thus, J_C and J_L should both vanish in this material, contrary to our measurements. Therefore, the observation of both a position-dependent LPGE in the 1T' and T_d phases and a CPGE only in the T_d phase indicates an unconventional origin of both PGEs.

The sign of J_C reverses in the T_d -phase MoTe₂ under illumination on the two sides of the electrodes (Table 1), suggesting the possibility that the CPGE current is circulating. To verify this, we designed a multi-electrode device arranged in a circle with the laser focused at the centre with a fixed spot size (Fig. 2a) on the room-temperature WSM $Mo_{0.9}W_{0.1}Te_2$. With the laser spot fixed at the centre of the circle defined by the electrodes, the photocurrent was collected between each of the nearest electrode pairs around the laser spot in the sequence $a\rightarrow b$, $b\rightarrow c$, $c\rightarrow d$, $d\rightarrow e$ and $e\rightarrow a$ (Fig. 2). Importantly, we observed that J_C is positive between all electrode pairs under right circularly polarized (RCP) light illumination and negative under left circularly polarized (LCP) light illumination, demonstrating that J_C circulates clockwise on RCP excitation and reverses

the winding direction under LCP excitation. This phenomenon was also confirmed in the low-temperature Weyl phase of MoTe₂ (Supplementary Figs. 4 and 5).

The appearance of a CPGE current and its circulating character require a breaking of $C_{2\nu}$ symmetry. The polarization-controlled circulating current is unlikely to originate from spatial disorder due to defects, in-plane strain during exfoliation or formation of nanoscale junctions due to intermixing of different phases, since in all these cases, the current would flow in random directions depending on the direction of the local symmetry breaking. The possibility of CPGE current flowing along the edges of the sample³² can also be eliminated as we have focused the light spot near the centre of the sample and the sample size is approximately ten times bigger than the spot diameter. However, a spatially inhomogeneous optical excitation due to a focused Gaussian beam profile can effectively break the internal point symmetry to produce a CPGE. This can be understood by analysing the dependence of the CPGE on spatial gradients of the optical field profile. We refer to the first-order term in the gradient expansion as the s-CPGE response and denote the local s-CPGE current as **j**_{sCPGE}.

In a further test of the dependence of the s-CPGE on the beam profile, experiments were performed on $\mathrm{Mo_{0.9}W_{0.1}Te_2}$ at room temperature, where the beam position was varied while keeping the beam size fixed. When the laser spot was continuously scanned along the perpendicular bisector of the two electrodes (along $\hat{\mathbf{y}}$) from one side to the other (Fig. 3a), J_{C} was zero when the laser spot lay at the midpoint of two electrodes, and changed polarity when the spot moved from the positive to the negative $\hat{\mathbf{y}}$ direction. This observation demonstrates that indeed a spatially varying optical beam profile effectively lowers the point symmetry, while the $C_{2\nu}$ symmetry is preserved when the Gaussian beam is centred between the electrodes. Another signature of s-CPGE current (Fig. 3b) was observed on varying the spot size while keeping the beam position fixed. The amplitude of J_{C} decreased when the spot size was increased and the field gradients were decreased. Also, for large

electrode separation compared with spot size, $I_{\rm C}$ again decreased because the circulating current cannot be collected at the electrodes. All these experiments indicate that the observed strong s-CPGE can be controlled by the optical beam profile.

A related photocurrent response has been observed in some III–V quantum-well systems manifesting as the inverse spin Hall effect³³. However, the spin is not conserved after optical excitation in general strongly spin–orbit coupled systems such as $MoTe_2/Mo_xW_{1-x}Te_2$. To understand the origin of the s-CPGE, a theory for a spatially dispersive contribution to $\mathbf{j}_{\text{sCPGE}}$ is derived (Supplementary Note 1):

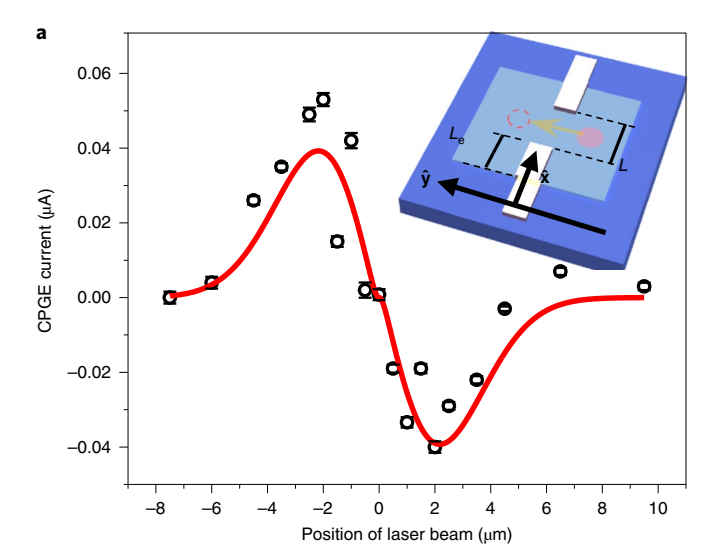
$$\mathbf{j}_{\text{sCPGE}}^{i}(\mathbf{r}) = \sum_{\mathbf{q}} \mathbf{j}_{\text{sCPGE}}^{i}(\mathbf{q}) e^{2i\mathbf{q}\cdot\mathbf{r}}$$

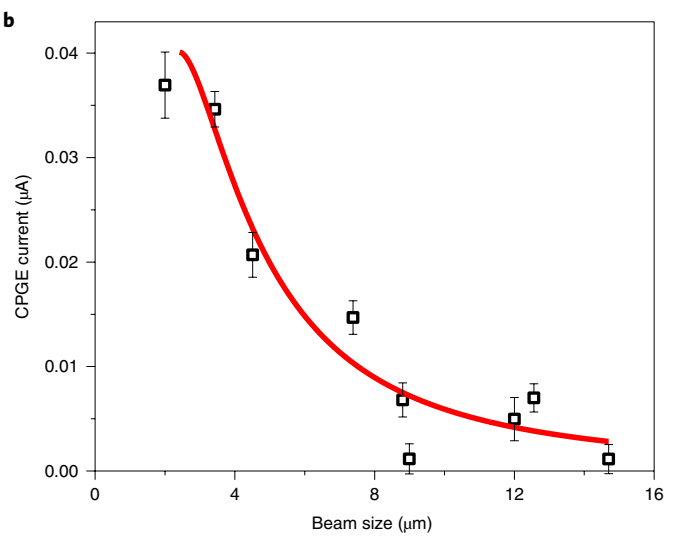
$$= \beta_{ilj} \sum_{\mathbf{q}} q_{l}(\mathbf{E}(\mathbf{q}, \omega) \times \mathbf{E}(\mathbf{q}, -\omega))_{j} e^{2i\mathbf{q}\cdot\mathbf{r}}$$
(2)

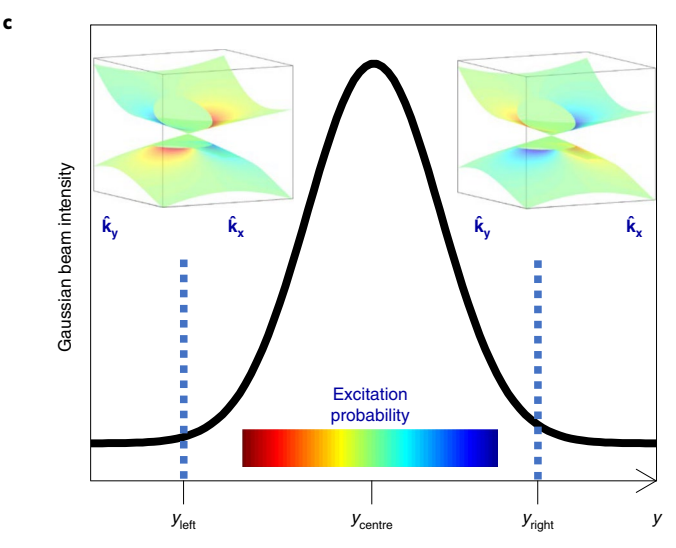
where β is a third-rank nonlinear conductivity tensor (tensor elements are described with subscripts i, j, l, q is the wave vector associated with the spatial gradient of the optical field and ω is the optical frequency. The electric field of a Gaussian beam with photon energy $\hbar\omega$, where \hbar is Planck's constant/ 2π , in real space is $\mathbf{E}(\mathbf{r},t) = \sum_{\mathbf{q},\omega} \mathbf{E}_0(\mathbf{q},\omega) \, \mathrm{e}^{i\omega t} \mathrm{e}^{i\mathbf{q}\cdot\mathbf{r}} \propto \mathrm{e}^{-(\mathbf{r}-\mathbf{r}_\mathrm{g})^2/w^2}$, where $\mathbf{r}-\mathbf{r}_\mathrm{g}$ is the radial coordinate of \mathbf{r} relative to the spot centre \mathbf{r}_{e} , and w is the Gaussian beam width. Using the equation of continuity, the circulating CPGE current arises from the transverse part of $\mathbf{j}_{\text{sCPGE}}$, produced by the antisymmetric term in the conductivity: $\sigma_{ilj} = \frac{1}{2} (\beta_{ili} - \beta_{lij})$. The direction of the transverse current $\hat{\mathbf{j}}_{sCPGE}$ is then determined by the direction of \mathbf{q} and the propagation direction of the optical field $\hat{\mathbf{n}}$ ($\hat{\mathbf{n}}$ is defined by $i\hat{\mathbf{E}} \times \hat{\mathbf{E}}^*$, where $\hat{\mathbf{E}}^*$ is the complex conjugate of $\hat{\mathbf{E}}$): $\hat{j}_{\text{sCPGE}} = \hat{q} \times \hat{n}$. Here, q is in the radial direction, and its magnitude follows the distribution obtained via a Fourier transform of the twodimensional Gaussian beam profile, while $\hat{\bf n}$ is along the light propagation direction, that is, $\pm \hat{\mathbf{z}}$. Therefore, $\mathbf{j}_{\text{sCPGE}}$ circulates around the beam centre with an amplitude proportional to the length of q and a sign determined by the photon helicity, as observed experimentally.

Fig. 3 | Spatial location and Gaussian spot size dependence of the s-CPGE current in $Mo_{0.9}W_{0.1}Te_2$ at room temperature. a, J_C as a function of the laser beam position. Black circles are the experimental data, and the red line is the fitting curve to the electrostatic model (Supplementary Note 2). Inset: schematic of the spatially dependent photocurrent measurement on $Mo_{0.9}W_{0.1}Te_2$ ($\hat{\mathbf{x}}-\hat{\mathbf{y}}$ plane). The laser beam (spot size $\approx 2 \,\mu\text{m}$) was scanned along the $\hat{\mathbf{y}}$ axis (yellow arrow). L_{e} is the total electrode length on the sample, and L is the separation between the two electrodes. **b**, J_c plotted as a function of the Gaussian beam diameter at a fixed distance y_0 to the electrodes in a. Black squares are the experimental data, and the red line is the fitting curve to the expression derived from the phenomenological model of $\mathbf{j}_{\text{sCPGE}}$. In **a** and **b**, error bars are the standard deviations of the fitted CPGE component from measured photocurrent data. c, Schematic of asymmetric interband excitation by a Gaussian beam, where the band touching points are located along the $\hat{\mathbf{x}}$ axis, and light propagates in the **2** direction. Main: spatial intensity distribution of a Gaussian beam along the $\hat{\mathbf{y}}$ axis, with y_{centre} being the y coordinate of the Gaussian beam centre. Inset: local excitation patterns contributing to s-CPGE current in the momentum space ($\hat{\mathbf{k}}_{\mathbf{x}'}$, $\hat{\mathbf{k}}_{\mathbf{y}}$ are the basis vectors) at the left (\mathbf{y}_{left}) and right (y_{right}) tails of the Gaussian beam. The colour map shows the normalized difference between the excitation probability (non-equilibrium electron population) under RCP and LCP light illumination. A negative value (blue region) implies that in comparison to homogeneous excitation, the optical field gradient results in fewer electrons being excited, while a positive value (red) implies excitation of more electrons.

The measured photocurrent magnitude can be related to $\mathbf{j}_{\text{sCPGE}}$ by a geometric factor associated with the electrode positions and is captured by a simple electrostatic model (Supplementary Note 2 and Supplementary Fig. 6). Both the dependence of J_{C} on spot location (Fig. 3a) and Gaussian beam width (Fig. 3b) can be well reproduced by our model, indicating that the phenomenological expression is consistent with the experimental data.







To develop a general microscopic description for the observed s-CPGE, we studied the semiclassical quantum density matrix $\rho(r,k,t)$ to first order in spatial field gradients and second order in the electric field within a nonlinear susceptibility framework³⁴ (Supplementary Note 3). The general quantum kinetic equation³⁵ is obtained from the equation of motion for the Wigner transformation for ρ , which includes the spatial inhomogeneity of ρ through the electric field driving term. Analogous to the injection current³⁶ in a homogeneous system, the derived steady-state response functions of $\mathbf{j}_{\text{sCPGE}}$ consist of $\rho^{(2)}$ quadratic in \mathbf{E} and linear in \mathbf{q} , and the band diagonal velocity, $v_{nn} = \frac{\partial e_n(\mathbf{k})}{\partial \mathbf{k}}$, with $\varepsilon_n(\mathbf{k})$ being the energy of band n at Bloch momentum \mathbf{k} . The two terms that control $\boldsymbol{\beta}$ for $\mathbf{j}_{\text{sCPGE}}$ for electronic interband transitions in equation (2) are (Supplementary Note 4)

$$\beta_{ilj,1} = \sum_{\mathbf{k},n,m} \frac{ie^{3}}{2\hbar^{2}} (\Gamma_{nm}(\omega) + \Gamma_{mn}(-\omega))$$

$$(f_{0}(\varepsilon_{m}) - f_{0}(\varepsilon_{n})) \Omega_{nm}^{j}(k) (v_{nn}^{l} v_{nn}^{i} \tau_{nn}^{2} - v_{mm}^{l} v_{mm}^{i} \tau_{mm}^{2})$$

$$(3)$$

$$\beta_{ilj,2} = \sum_{\mathbf{k},n,m} \frac{e^3}{8\hbar} \left(\Gamma_{nm}^2(\omega) + \Gamma_{mn}^2(-\omega) \right) \left(f_0(\varepsilon_m) - f_0(\varepsilon_n) \right)$$

$$\Omega_{nm}^j(k) \left(v_{nn}^l + v_{mm}^l \right) \left(v_{nn}^i \tau_{nn} - v_{mm}^i \tau_{mm} \right)$$

$$(4)$$

where $f_0(\varepsilon_n(\mathbf{k}))$ is the Fermi–Dirac distribution, $\tau_{nn}(\mathbf{k})$ is the relaxation time of excited carriers in band n, $\Gamma_{nm}(\mathbf{k},\omega) = \frac{1}{\hbar\omega + \varepsilon_n - \varepsilon_m - \frac{i\hbar}{\varepsilon_{nm}}}$

and $\Omega_{nm}^{i}(\mathbf{k}) = -i(R_{nm}^{j}R_{mn}^{k} - R_{nm}^{k}R_{mn}^{j})$ is derived from interband matrix elements of the non-diagonal Berry connection, $R_{nm}(\mathbf{k})$. This quantity transforms like the Berry curvature, $\Omega_{nm}^{i}(\mathbf{k}) = \Omega_{nm}^{i}(-\mathbf{k})$ under inversion symmetry and $\Omega_{nm}^{i}(\mathbf{k}) = -\Omega_{nm}^{i}(-\mathbf{k})$ under time reversal symmetry, so that it is allowed only if time reversal or inversion symmetry is broken. Although part of the full response function has no symmetry restrictions, the dominating part (equations (3) and (4)) would vanish under inversion symmetry. Therefore, the expressions explain why a s-CPGE does not exist in the 1T' phase of MoTe₂ but arises only after a temperature- or doping-induced phase transition to the broken-inversion T_d phase. Quantitatively, the magnitude of $\mathbf{j}_{s,CPGE}$ is sensitive to band dispersion, since these response functions carry two orders of the band diagonal velocities, and is also closely related to the band-resolved Berry curvatures $\Omega_{nm}^{i}(\mathbf{k})$ involved in transitions.

This microscopic description of the s-CPGE response requires controlling the **k**-space distribution of excited electrons using optical field gradients, in contrast to a conventional CPGE, which depends only on the polarization of a spatially uniform optical field. The mechanism is illustrated by the excitation in the Weyl cone under Gaussian beam illumination, shown in Fig. 3c. The excitation probability under circularly polarized light at two different spatial locations of the Gaussian beam are different, that is, opposite regions of the Weyl cone are excited when the local ${\bf q}$ is reversed, which is reflected in the s-CPGE polarity (current circulation direction). Therefore, we can expect that interaction of the Weyl fermions with the optical field controlled by the beam profile can be probed by the s-CPGE under low-frequency excitations.

To further study the s-CPGE under low-frequency excitations near the Weyl nodes quantitatively, we calculated our response functions using a minimal model of a WSM (Supplementary Note 5). On adding a small inversion-breaking term controlled by the parameter L_0 on a 4×4 Hamiltonian describing a three-dimensional Dirac semimetal³⁷

$$\begin{array}{rcl} H_{\Gamma}\left(\mathbf{k}\right) & = & \varepsilon_{0}\left(\mathbf{k}\right) + M\left(\mathbf{k}\right)l \otimes \tau_{z} + \\ & & Ak_{x}\sigma_{z} \otimes \tau_{x} - Ak_{y}l \otimes \tau_{y} + L_{0}k_{z}\sigma_{z} \otimes \tau_{z} \end{array} \tag{5}$$

where $\varepsilon_0(\mathbf{k}) = C_0 + C_1 k_z^2 + C_2 (k_x^2 + k_y^2)$, $k_\pm = k_x \pm i k_y$ and $M(\mathbf{k}) = M_0 - M_1 k_z^2 - M_2 (k_x^2 + k_y^2)$, $(M_0, M_1, M_2, C_0, C_1, C_2, A)$ are the model parameters), the new Hamiltonian describes a WSM with four Weyl points separated along the $\hat{\mathbf{k}}_z$ axis (Fig. 4a). The nonvanishing $\Omega_{nm}^i(\mathbf{k})$ produces a non-zero $\mathbf{j}_{\text{SCPGE}}$, and the transverse part of the conductivity, σ_{zyx} , as a function of ω is shown in Fig. 4b. Numerical analysis shows that $\sigma(\omega)$ scales as $\frac{\alpha\omega + \alpha'\omega^2}{1 + \beta\omega^3 + \beta'\omega^4}$ (where

 α , α' , β and β' are fitting parameters). When the Fermi level is above the Lifshitz energy (but still below the energy cut-off), σ grows linearly with slope α due to Pauli blocking at small frequencies and reaches a maximum at photon frequency $\omega_p = \frac{1}{(2R)^3}$, followed by

 ω^{-2} scaling at the high-frequency tail. This behaviour is different from a conventional CPGE where, instead, $\sigma(\omega)$ scales as ω^{-1} at high frequencies (Supplementary Fig. 7). However, when the Fermi level is lower than the Lifshitz energy, $\sigma_{\rm syx}$ changes its sign at a certain frequency determined by the chemical potential, which happens due to band crossing in WSMs. From the response functions, transitions at low photon frequencies tuned between the crossed bands would have a different polarity of the band-resolved Berry curvatures and contribute to the s-CPGE conductivity with a different sign compared with transitions at higher frequencies above the Lifshitz energy. The sign reversal would be particularly prominent for type-II WSMs where the tipping of Weyl cones favours transitions in the band-crossing region at low energies. This feature could be extremely useful in probing topological semimetals, whose main characteristics include band crossings near the Fermi level.

To examine the predicted capability of using the s-CPGE as a probe of WSMs, s-CPGE experiments were performed on ${\rm Mo_{09}W_{0.1}Te_2}$ (Weyl phase) with a 6.2 µm laser at room temperature, which excites in the vicinity of the Weyl nodes (Supplementary Fig. 8). The photocurrent was measured at three spots (Fig. 4c inset), that is, bottom-left side (spot a), top-right side (spot b) and the midpoint of the electrodes (spot c). The characteristic of the measured photocurrent agrees qualitatively with the 750 nm measurements, as the CPGE current is negative at spot a, positive at spot b and vanishes at spot c (see also Supplementary Fig. 9). This shows that the s-CPGE response also exists under low-energy excitations with qualitatively similar characteristics as 750 nm (Fig. 4d inset and Fig. 3b).

However, by comparing the experimentally measured $J_{\rm C}$ at spot a and spot b, the polarity of the s-CPGE current measured at 750 nm (~1.65 eV) and that at 6.2 µm (~0.2 eV) on the same sample were found to be opposite (Fig. 4c,d). In other words, the circulating s-CPGE current at the two excitation wavelengths have opposite signs, as predicted by our model. To obtain a more complete behaviour of the s-CPGE response, especially to find the energy at which the sign reversal occurs, more measurements were carried out over a broad wavelength range, that is, 1,400–1,950 nm. As shown in Fig. 4e, the sign of the s-CPGE current was found to reverse at ~1,850 nm (0.67 eV) and then maintain its sign at higher excitation energies (~1.18–1.65 eV) (Supplementary Fig. 10).

The experimental results were then compared with first-principle calculations on the T_d phase of MoTe₂. In these band calculations, the s-CPGE current as a function of photon energy shows a similar trend as predicted by the minimal model (Fig. 4f); that is, the current first gradually increases to reach a maximum at a certain energy, and then decreases to eventually reverse its sign. We find that the energy at which the sign reversal occurs depends strongly on the average asymmetric relaxation time (Supplementary Fig. 11), and fitting to the experimental data gives an estimation of ~2×10⁻¹⁵ s. Unlike a conventional injection current, momentum-space asymmetry in the electron scattering rate is crucial for the existence of a s-CPGE since only the antisymmetric contribution to the relaxation time, $\tau_{nm}(-\mathbf{k})^{(asy)} = -\tau_{nm}(\mathbf{k})^{(asy)}$ (n, m are band indices) can give rise to non-zero β_1 or β_2 . In general, the scattering probability function

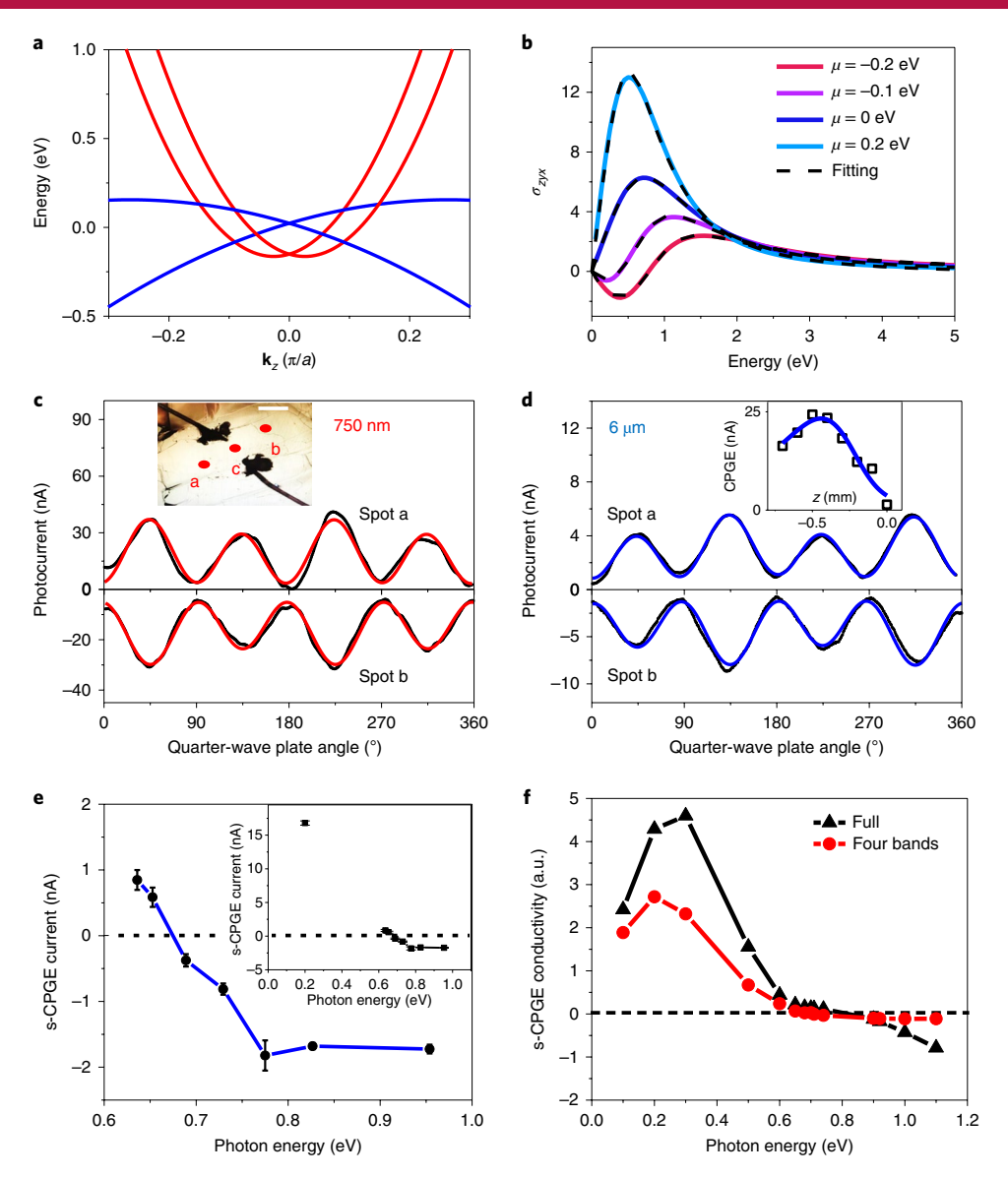


Fig. 4 | Numerical and experimental results for s-CPGE current over a broad wavelength range (visible to mid-infrared). a, Band structure of inversion-broken WSM obtained from a model Dirac semimetal by adding an inversion-breaking term from equation (5), which consists of two conduction (red) and two valence bands (blue), a in the unit denotes a direct space lattice parameter. **b**, Plots of the σ_{zyx} of the WSM as a function of ω at different Fermi energies

 μ and fittings to the scaling function $\frac{\alpha\omega + \alpha'\omega^2}{1+\beta\omega^3+\beta'\omega^4}$. **c**, Photocurrents measured with a 750 nm laser, plotted as a function of φ at spots a and b. Black dots are the experimental data, and red lines are the fits to equation (1). Inset: optical image of the Mo_{0.9}W_{0.1}Te₂ device, in which the sample (white surface) is connected with two metal wires (black lines) by silver paste (two black spots), and the three red spots indicate the three beam positions at which polarization-dependent photocurrent measurements were performed. Scale bar: 200 μ m. **d**, Photocurrents measured by a 6 μ m laser, plotted as a function of φ at spots a and b. Black dots are the experimental data, and blue lines are the fits to equation (1). Comparing data at the same fixed spot (between **c** and **d**) clearly shows that the photocurrent reverses polarity for excitation at 6.2 μ m and 750 nm for s-CPGE response, in accordance with our model in **c**. Inset: with the 6.2 μ m laser beam fixed at spot a, s-CPGE current plotted as a function of change in distance between focusing objective and sample plane (denoted by z, and the working distance of the objective is taken as zero) and fitted by the phenomenological model, demonstrating that the response is qualitatively similar to 750 nm (Fig. 3b). The Gaussian beam width obtained from the fitting parameter is in accordance with the real spot size (-80 μ m), which shows that the phenomenological mechanism of the s-CPGE is similar over a broad spectral range. **e**, Measured s-CPGE current magnitude at different wavelengths (1,400-1,950 nm) on the same Mo_{0.9}W_{0.1}Te₂ device as **b** and **c**. Inset: s-CPGE current magnitude at 6.2 μ m, included for rough comparison. Error bars are the standard deviations of the fitted CPGE component from measured photocurrent data. **f**, The s-CPGE conductivity calculated for the Weyl phase of Mo and ρ orbitals of Te. The red curve represents the s-CPGE conductivity calculated from the four bands closest to the Fermi level.

follows the crystal symmetry³⁸, so an antisymmetric modulation of the relaxation time of \mathbf{k} is allowed only in the broken-inversion phase in these materials. Furthermore, when large spin–orbit coupling is present, spin-dependent skew scattering^{39–41} at positive and

negative \mathbf{k} states occurs with different probabilities (that is, scattering probability $W_{\mathbf{k}k'} \neq W_{\mathbf{k}'\mathbf{k}}$) and would augment an isotropic scattering rate by an antisymmetric contribution, which is the main contribution to $\tau_{nm}(\mathbf{k})^{(asy)}$. The experimentally measured positive correlation

between the s-CPGE and temperature (Supplementary Fig. 5), which differs from most conventional CPGE²⁸ responses, is one of the technique's special features arising from this unique mechanism.

The s-CPGE conductivity calculated from only the four bands near the Fermi energy can reproduce a large portion of the full s-CPGE conductivity over a broad frequency range (Fig. 4f), and the sign reversal of the s-CPGE can be reproduced by using only the four bands forming the Weyl points. This implies that the sign reversal can be mostly attributed to these four bands, and as illustrated in the four-band model analysis, is a result of band inversion. With good agreement between the experimental data and minimal model and first-principles calculations, the s-CPGE sign reversal is evidence of band crossings in MoTe₂/Mo_xW_{1-x}Te₂ systems. Furthermore, a large enhancement of the s-CPGE coefficient at 6.2 µm (Fig. 4e inset; see also Supplementary Fig. 12) can be attributed to the Berry curvature monopoles and antimonopoles at the Weyl points (Supplementary Note 6). Therefore, our results demonstrate that the s-CPGE is a promising technique that can probe the unique characteristics of topological systems.

In conclusion, an s-CPGE with a photon helicity-dependent circulating photocurrent is observed in type-II WSMs MoTe₂ and Mo_{0.9}W_{0.1}Te₂. The derived nonlinear susceptibilities encode the effects of spatially inhomogeneous field excitation and explain the existence of the s-CPGE in WSMs. Using low-energy excitation, we controlled the asymmetric carrier excitation near Weyl nodes by optical field gradients. Through a comprehensive comparison between wavelength-dependent measurements and calculations, we found evidence of Berry curvature singularities, discussed the effect of band inversion on the sign reversal of the s-CPGE response and demonstrated the potential of the technique to probe the topological band properties and carrier relaxation dynamics of symmetry-broken materials. Our work also demonstrates that precisely tailored photon spin-dependent optoelectronic responses can be engineered in these systems by shaping and patterning optical field profiles, which can greatly enhance the applications of topological materials over a broad spectral range.

Online content

Any methods, additional references, Nature Research reporting summaries, source data, statements of code and data availability and associated accession codes are available at https://doi.org/10.1038/s41563-019-0421-5.

Received: 18 February 2018; Accepted: 4 June 2019; Published online: 15 July 2019

References

- 1. Kane, C. L. & Mele, E. J. Z_2 topological order and the quantum spin Hall effect. *Phys. Rev. Lett.* **95**, 146802 (2005).
- Hasan, M. Z. & Kane, C. L. Colloquium: topological insulators. Rev. Mod. Phys. 82, 3045–3067 (2010).
- Qi, X.-L. & Zhang, S.-C. Topological insulators and superconductors. Rev. Mod. Phys. 83, 1057–1110 (2011).
- Wan, X., Turner, A. M., Vishwanath, A. & Savrasov, S. Y. Topological semimetal and Fermi-arc surface states in the electronic structure of pyrochlore iridates. *Phys. Rev. B* 83, 205101 (2011).
- Armitage, N., Mele, E. & Vishwanath, A. Weyl and Dirac semimetals in three-dimensional solids. Rev. Mod. Phys. 90, 015001 (2018).
- 6. Soluyanov, A. A. et al. Type-II Weyl semimetals. Nature 527, 495-498 (2015).
- Burkov, A. & Balents, L. Weyl semimetal in a topological insulator multilayer. Phys. Rev. Lett. 107, 127205 (2011).
- Nielsen, H. B. & Ninomiya, M. The Adler–Bell–Jackiw anomaly and Weyl fermions in a crystal. *Phys, Lett. B* 130, 389–396 (1983).
- Zyuzin, A. & Burkov, A. Topological response in Weyl semimetals and the chiral anomaly. *Phys. Rev. B* 86, 115133 (2012).
- Potter, A., Kimchi, I. & Vishwanath, A. Quantum oscillations from surface Fermi arcs in Weyl and Dirac semimetals. *Nat. Commun.* 5, 5161 (2014).
- Hosur, P. & Qi, X.-L. Recent developments in transport phenomena in Weyl semimetals. CR Phys. 14, 857–870 (2013).

- Xiong, J. et al. Evidence for the chiral anomaly in the Dirac semimetal Na₃Bi. Science 350, 413–416 (2015).
- Ma, Q. et al. Direct optical detection of Weyl fermion chirality in a topological semimetal. Nat. Phys. 13, 842–847 (2017).
- Wu, L. et al. Giant anisotropic nonlinear optical response in transition metal monopnictide Weyl semimetals. Nat. Phys. 13, 350–355 (2017).
- Morimoto, T., Zhong, S., Orenstein, J. & Moore, J. E. Semiclassical theory of nonlinear magneto-optical responses with applications to topological Dirac/ Weyl semimetals. *Phys. Rev. B* 94, 245121 (2016).
- Chan, C.-K., Lindner, N. H., Refael, G. & Lee, P. A. Photocurrents in Weyl semimetals. *Phys. Rev. B* 95, 041104 (2017).
- König, E., Xie, H.-Y., Pesin, D. & Levchenko, A. Photogalvanic effect in Weyl semimetals. Phys. Rev. B 96, 075123 (2017).
- Zhang, Y., Sun, Y. & Yan, B. Berry curvature dipole in Weyl semimetal materials: an ab initio study. *Phys. Rev. B* 97, 041101 (2018).
- de Juan, F., Grushin, A. G., Morimoto, T. & Moore, J. E. Quantized circular photogalvanic effect in Weyl semimetals. *Nat. Commun.* 8, 15995 (2017).
- Wang, Z. et al. MoTe₂: a type-II Weyl topological metal. Phys. Rev. Lett. 117, 056805 (2016).
- Huang, L. Spectroscopic evidence for a type-II Weyl semimetallic state in MoTe₂. Nat. Mater. 15, 1155–1160 (2016).
- Belopolski, I. et al. Discovery of a new type of topological Weyl fermion semimetal state in Mo.W_{1-x}Te₂. Nat. Commun. 7, 13643 (2016).
- Chang, T.-R. et al. Prediction of an arc-tunable Weyl Fermion metallic state in Mo_xW_{1-x}Te₂. Nat. Commun. 7, 10639 (2016).
- Zhang, K. et al. Raman signatures of inversion symmetry breaking and structural phase transition in type-II Weyl semimetal MoTe₂. Nat. Commun. 7, 13552 (2016).
- Deng, K. et al. Experimental observation of topological Fermi arcs in type-II Weyl semimetal MoTe₂. Nat. Phys. 12, 1105–1110 (2016).
- Belopolski, I. et al. Topological Weyl phase transition in Mo_xW_{1-x}Te₂. Preprint at https://arxiv.org/abs/1612.07793 (2016).
- Dhara, S., Mele, E. J. & Agarwal, R. Voltage-tunable circular photogalvanic effect in silicon nanowires. Science 349, 726–729 (2015).
- McIver, J., Hsieh, D., Steinberg, H., Jarillo-Herrero, P. & Gedik, N. Control over topological insulator photocurrents with light polarization. *Nat. Nanotech.* 7, 96–100 (2012).
- Ivchenko, E. & Ganichev, S. in Spin Physics in Semiconductors (ed. Dyakonov, M. I.) Ch. 9 (Springer, 2008).
- Ganichev, S. D. & Prettl, W. Spin photocurrents in quantum wells. J. Phys. Condens. Matter 15, R935–R983 (2003).
- Shalygin, V., Moldavskaya, M., Danilov, S., Farbshtein, I. & Golub, L. Circular photon drag effect in bulk tellurium. *Phys. Rev. B* 93, 045207 (2016).
- Karch, J. et al. Terahertz radiation driven chiral edge currents in graphene. Phys. Rev. Lett. 107, 276601 (2011).
- He, X. et al. Anomalous photogalvanic effect of circularly polarized light incident on the two-dimensional electron gas in Al_xGa_{1-x}N/GaN heterostructures at room temperature. *Phys. Rev. Lett.* 101, 147402 (2008).
- Sipe, J. & Shkrebtii, A. Second-order optical response in semiconductors. *Phys. Rev. B* 61, 5337–5352 (2000).
- Sekine, A., Culcer, D. & MacDonald, A. H. Quantum kinetic theory of the chiral anomaly. *Phys. Rev. B* 96, 235134 (2017).
- Sturman, P. J. Photovoltaic and Photo-refractive Effects in Noncentrosymmetric Materials Vol. 8 (CRC Press, 1992).
- Wang, Z. et al. Dirac semimetal and topological phase transitions in A₃Bi (A = Na, K, Rb). Phys. Rev. B 85, 195320 (2012).
- 38. Olbrich, P. et al. Room-temperature high-frequency transport of Dirac fermions in epitaxially grown Sb₂Te₃- and Bi₂Te₃-based topological insulators. *Phys. Rev. Lett.* **113**, 096601 (2014).
- 39. Hirsch, J. Spin Hall effect. Phys. Rev. Lett. 83, 1834-1837 (1999).
- 40. Rubin, L. & Sample, H. *The Hall Effect and Its Applications* (Plenum Press, 1980).
- Deyo, E., Golub, L., Ivchenko, E. & Spivak, B. Semiclassical theory of the photogalvanic effect in non-centrosymmetric systems. Preprint at https:// arxiv.org/abs/0904.1917 (2009).

Acknowledgements

R.A. acknowledges the support from the Office of Naval Research MURI (grant no. N00014-17-1-2661), US Army Research Office (grant no. W911NF-17-1-0436) and the RAISE-EQuIP-NSF-ECCS-1842612 grant from the NSF (USA). Calculation of the s-CPGE response by E.J.M. and Z.A. was supported by the Department of Energy (grant no. DE FG02 84ER45118). The crystal growth effort (P.Y. and Z.L.) was supported by the Singapore National Research Foundation under NRF RF Award No. NRF-RF2013-08 and Tier 2 MOE2016-T2-2-153. A.M.R. acknowledges support from the US Department of Energy, Office of Science, Basic Energy Sciences Program under grant DE-FG02-07ER46431. R.A., C.L.K. and A.M.R. acknowledge the support from the Penn's MRSEC Seed Grant (DMR-1720530). Computational support was provided by the National Energy Research Scientific Computing Center of the DOE.

Author contributions

R.A. supervised the project. Z.J. and R.A. conceived and designed the project and experiments. Z.J. and G.L. performed all the measurements with some assistance from W.L.; Z.J. and G.L. fabricated the devices and analysed the data with R.A.; Z.J. and Z.A. developed the microscopic theory under the supervision of E.J.M. and C.L.K.; Z.J. performed realband calculations with the help of H.G. and A.M.R.; P.Y. and Z.L. grew the single crystals on which all the optoelectronic measurements were performed. Z.J., R.A. and E.J.M. wrote the manuscript. All the authors discussed the results and commented on the manuscript.

Competing interests

The authors declare no competing interests.

Additional information

Supplementary information is available for this paper at https://doi.org/10.1038/s41563-019-0421-5.

Reprints and permissions information is available at www.nature.com/reprints.

Correspondence and requests for materials should be addressed to R.A.

 $\label{Publisher's note:} \textbf{Publisher's note:} \ \textbf{Springer Nature remains neutral with regard to jurisdictional claims in published maps and institutional affiliations.}$

© The Author(s), under exclusive licence to Springer Nature Limited 2019

Methods

Growth of single crystals. Large, well-formed, ribbon-like single crystals of MoTe₂, Mo_{0.9}W_{0.1}Te₂ and Mo_{0.3}W_{0.7}Te₂ alloy were grown by chemical vapour transport with iodine (I) as the carrier gas. Stoichiometric amounts of W powder (99.9%, Sigma-Aldrich), Mo powder (99.95%, Sigma-Aldrich) with a total weight of 500 mg, plus an extra 35 mg of I as the transport gas were sealed in an evacuated 20 cm-long quartz tube under vacuum at 10^{-6} torr. The quartz tube was placed in a three-zone furnace. First, the reaction zone was maintained at 850 °C for 30 h with the growth zone at 900 °C to prevent the transport of the product and a complete reaction; then the reaction zone was heated to 1,070 °C and held for 7 d with the growth zone at 950 °C. Finally, the furnace was naturally cooled down to room temperature and the single crystals were collected in the growth zone. Residual I was cleaned using acetone before measurement.

Device fabrication. Devices were fabricated on exfoliated MoTe₂, Mo_{0.9}W_{0.1}Te₂ and Mo_{0.3}W_{0.7}Te₂ flakes with thicknesses of ~100–300 nm and typical dimensions of $20\,\mu\text{m}\times20\,\mu\text{m}$ on SiO₂/Si substrates. Electrodes were defined by electron beam lithography followed by physical vapour deposition of 300 nm Ti/100 nm Au film.

Photocurrent measurements. Three excitation sources were used in this study: a Ti-sapphire pulsed laser (Coherent) in the 680-1,080 nm wavelength range, a supercontinuum laser (NKT Photonics) in the 400-2,200 nm range and a quantum cascade laser (Daylight Solutions) in the 6.0– $6.2\,\mu m$ range. The Ti-sapphire laser was focused to a near-perfect Gaussian spot by a ×60 objective, and the full-width at half-maximum of the spot was controlled in the range of ~2-20 µm, with total power in the 1-12 mW range. The supercontinuum laser beam was focused by an aspheric lens, and the quantum cascade laser was focused by an objective with $\sim\!80\,\mu m$ full-width at half-maximum at 6.2 μm . For all measurements, the quarter-wave plate appropriate for each wavelength mounted on a motorized precision rotation stage driven by a servo motor (Thorlabs) was used to vary the angle continuously from 0° to 360° to obtain different laser polarizations. The laser polarization on the sample plane was analysed carefully to ensure accuracy. The power difference between the LCP and RCP light was measured by the power meter to be less than 1%, and the extinction ratio of linearly polarized light was ensured to be larger than 1,000:1. When scanning the light beam over the sample using piezoelectric stages, the spatial coordinates were recorded with an accuracy of ~200 nm. Photocurrents (Figs. 1-3) were recorded using a current preamplifier (DL Instruments model 1211) for which the output signal (the photocurrent was converted to an amplified voltage signal) was recorded continuously (approximately ten data points per second) by the Peripheral Component

Interconnect (PCI) card (National Instruments, PCI-6281). The time constant of the preamplifier was chosen in the range of 100–300 ms. In other measurements, photocurrents were recorded using a lock-in amplifier (Stanford Research Systems, SR860)²⁷.

First-principle calculations. The electronic band structures were calculated with Quantum Espresso⁴² by using generalized gradient approximation pseudopotentials⁴³ for Mo and Te. Spin–orbit coupling was included in the pseudopotentials, and the Perdew–Burke-Ernzerhof approximation was used. Self-consistent field calculations were performed on a $10\times4\times4$ gamma-point-centred k-point grid, with a Gaussian smearing width of $0.01\,\mathrm{eV}$. The energy cut-off was chosen at 50 rydberg (Ry). Additional calculations were performed using a $6\times6\times4\,\mathrm{k}$ -point grid, with an energy cut-off of 50 Ry, also using a Gaussian smearing width of $0.01\,\mathrm{eV}$. In the calculations, the experimental lattice parameters of MoTe₂ in the T_d phase were used, and band structure agrees well with previously reported calculations by Wang et al. ²⁰. For the tight binding model, a Wannier function interpolated band structure of Mo 4d and 5s and Te 5p orbitals was constructed ^{44,45}.

Data availability

The data presented in this study are available from the corresponding author upon reasonable request.

Code availability

The code for calculating the s-CPGE in this study is available from the corresponding author upon reasonable request.

References

- Giannozzi, P. et al. QUANTUM ESPRESSO: a modular and open-source software project for quantum simulations of materials. J. Phys. Condens. Matter 21, 395502 (2009).
- Rappe, A. M., Rabe, K. M., Kaxiras, E. & Joannopoulos, J. Optimized pseudopotentials. *Phys. Rev. B* 41, 1227–1230 (1990).
- Souza, I., Marzari, N. & Vanderbilt, D. Maximally localized Wannier functions for entangled energy bands. *Phys. Rev. B* 65, 035109 (2001).
- 45. Mostofi, A. A. et al. wannier90: a tool for obtaining maximally-localised Wannier functions. *Comput. Phys. Commun.* **178**, 685–699 (2008).